# Chapter 13
# Acoustic Metamaterials for Sub-wavelength, Broadband, and Perfect Absorption in Ventilated Problems




**Vicent Romero-García, Noé Jiménez, Jean-Philippe Groby, and Vincent Pagneux**

**Abstract** This chapter describes the possibilities given by acoustic metamaterials to produce sub-wavelength, broadband, and perfect absorption in ventilated problems, i.e., accounting for both reflected and transmitted waves. We discuss the problem of perfect acoustic absorption both in the reflection and ventilated problems reviewing the different acoustic metamaterials described in the literature to achieve these two goals. The general one-dimensional reciprocal scattering problem is first considered to derive the rigorous perfect absorption conditions. The complex frequency plane and the Argand diagrams are then introduced to interpret and visualize the perfect absorption conditions. Acoustic metamaterials made of Helmholtz resonators are subsequently introduced, paying special attention to slow-sound systems. Finally, two examples of acoustic metamaterials based on these acoustic metamaterials are shown, exhibiting perfect absorption either with or without mirror symmetry.

V. Romero-García (✉)
Instituto Universitario de Matemática Pura y Aplicada (IUMPA), Universitat Politécnica de Valéncia, Camino de Vera s/n, 46022, Valéncia, Spain
e-mail: virogar1@mat.upv.es

J.-P. Groby · V. Pagneux
Laboratoire d'Acoustique de l'Université du Mans (LAUM), UMR CNRS 6613, Institut d'Acoustique—Graduate School (IA-GS), CNRS, Le Mans Université, Le Mans, France
e-mail: jpgroby@univ-lemans.fr

V. Pagneux
e-mail: vincent.pagneux@univ-lemans.fr

N. Jiménez
Instituto de Instrumentación para Imagen Molecular, Universitat Politècnica de València, Consejo Superior de Investigaciones Científicas, Camino de Vera s/n, 46085 València, Spain
e-mail: noe.jimenez@csic.es

© Springer Nature Switzerland AG 2024

R. Craster and S. Guenneau (eds.), *Acoustic Metamaterials*, Springer Series in Materials Science 345, https://doi.org/10.1007/978-3-031-60015-9_13

## 13.1 Introduction

Deep sub-wavelength perfect absorption is a scientific and technological challenge that requires to solve a complex twofold problem: reducing the dimensions of the structure while increasing the resonances at low frequencies with the good conditions to impedance match the system with the background medium. Both the universality and the possibility of perfect absorption makes it a fascinating topic for fundamental research and is at the heart of its technological relevance in different applications in the broad field of wave physics as in wave filtering, sensing, communications, energy harvesting, and thermal emission control [1, 2].

Metamaterials are good candidates to meet the required deep sub-wavelength character of such perfect absorbers [3]. Although the definition of metamaterial is still a source of discussion within the community, in this chapter, we will call metamaterial any structured system made up of resonant elements with physical properties not usually encountered for wavelengths much larger than its dimensions. Metamaterials have received increasing interest in electromagnetics [4], acoustics [5, 6], elastodynamics [7, 8], and seismology [9], among other fields in wave physics. In this chapter, we will pay attention to the case of acoustic metamaterials.

The concept of acoustic metamaterial was introduced in 2000 by Liu et al. [10] showing that locally resonant systems presented forbidden gaps at frequencies much lower than Bragg band gaps. These stop gaps were found to be associated to negative dynamic properties of the system when homogenization techniques were applied [11]. Although similar results were already obtained in the acoustics community several years before [12, 13], the interpretation of negative dynamic properties was a breakthrough introducing the concept of acoustic metamaterials [14]. Due to their locally resonant nature, these structures show deep sub-wavelength properties exploited to study fundamental phenomena [6], and are nowadays applied in many industrial applications [5, 15].

Several possibilities based on acoustic metamaterials have been recently proposed to design sound absorbing structures with simultaneous sub-wavelength dimensions and strong acoustic absorption [16–21]. Some strategies to design these sub-wavelength systems consist of using space-coiling structures [22–26], membranes [27, 28], reconfigurable structures [29, 30], or Helmholtz resonators (HRs) [12–14]. However, all of these structures face the challenge of impedance mismatch to the background medium while they bring potentially solutions to reduce the geometric dimensions.

In this chapter, we pay attention to the possibilities provided by the acoustic metamaterials to *perfectly* absorb waves with deep sub-wavelength dimensions in ventilated problems, i.e., in transmission problems in which we consider both reflected and transmitted waves. From a general point of view, perfect absorption can be analyzed from the interaction of an incoming wave with an open, lossy, and resonant structure. In particular, the impedance matching with the background field, is one of the most studied processes in the field of wave physics [31–33]. These open systems are characterized at their resonant frequency by both the leakage rate of energy

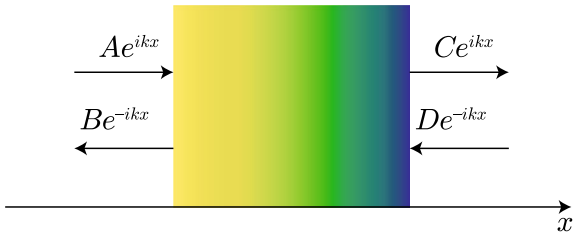



**Fig. 13.1** **a** 1D reciprocal scattering problem. $A$ and $D$ ($B$ and $C$) are the amplitudes of the incoming (outgoing) waves. We use the time convention of type $e^{-i\omega t}$. The graded color represents the non-mirror symmetric properties, being the more general case

(i.e., the coupling of the resonant elements with the propagating medium), and the intrinsic losses of the resonator. The balance between the leakage and the losses activates the condition of critical coupling (or impedance matching condition), trapping the energy around the resonant elements and generating a maximum of energy absorption [34, 35].

Recently, several possibilities based on these systems have been proposed to design sound absorbing structures with impedance match conditions presenting simultaneously sub-wavelength dimensions and perfect acoustic absorption. Several examples based on membrane-type or plate-type acoustic metamaterials [16, 28, 36–40], quarter wavelength resonators [41, 42], bubbles in water [43], aerogel plates [44], split ring resonators [45], graded porous materials [46], metaporous materials [19–21], or HRs [23, 28, 35, 47–63, 74] have been proposed in the last ten years. HRs have effectively been shown as potential candidates to solve the problem of sub-wavelength absorption due to the tunable possibilities they offer by just optimizing their geometry. Below, we will show the general conditions for perfect absorption illustrating them with different examples of acoustic metamaterials made up of HRs. In this type of acoustic metamaterials, the resonance frequency, the energy leakage, and the intrinsic losses can be passively tuned by adjusting the geometry of the resonators. In practice, the energy leakage of HRs can be controlled by the aperture of the neck, while the intrinsic losses can be controlled by the inherent viscothermal processes at its neck and cavity.

The chapter is organized as follows. In Sect. 13.2 the general problem of a reciprocal scattering problem will be discussed. We will provide explicitly the perfect absorption condition for mirror and non-mirror symmetric systems. In order to interpret and visualize the perfect absorption conditions, we will introduce two different techniques in Sect. 13.3: the complex frequency plane and the Argand diagram. Then, we will show examples of non-mirror and mirror symmetric perfect absorption by acoustic metamaterials made of HRs in Sect. 13.4. Finally, concluding remarks are summarized in Sect. 13.5.

## 13.2 Perfect Absorption Conditions

### *13.2.1 General 1D Reciprocal Scattering Problem*

Let us consider a two-port, one-dimensional, and reciprocal scattering process. We note that the reciprocity condition implies that the transmission coefficient obtained when excited from each side must be the same. The relation between the amplitudes of the incoming ($A$, $D$) and outgoing ($B$, $C$) waves on both sides of the system, considering $e^{-i\omega t}$ as the time dependence convention of the harmonic regime, as shown in Fig. 13.1, is given by

$$\begin{pmatrix} C \\ B \end{pmatrix} = \mathbf{S}(f) \begin{pmatrix} A \\ D \end{pmatrix} = \begin{pmatrix} T & R^+ \\ R^- & T \end{pmatrix} \begin{pmatrix} A \\ D \end{pmatrix}, \tag{13.1}$$

where $\mathbf{S}(f)$ is the scattering matrix (S-matrix), $f$ is the incident wave frequency, $T$ is the complex amplitude transmission coefficient, $R^-$ and $R^+$ are the complex amplitude reflection coefficients for left ($-$) and right ($+$) incidence, respectively. Note that the power scattering coefficients are, $|R^+|^2$, $|R^-|^2$ and $|T|^2$.

In the most general case, the scattering matrix can be written as

$$\begin{pmatrix} C \\ B \end{pmatrix} = \mathbf{S}(f) \begin{pmatrix} A \\ D \end{pmatrix} = \begin{pmatrix} T^+ & R^+ \\ R^- & T^- \end{pmatrix} \begin{pmatrix} A \\ D \end{pmatrix}.$$

Energy conservation and time reversal symmetry imply both the unitarity of the scattering matrix, i.e., $\mathbf{S}^\dagger\mathbf{S} = \mathbf{I}$, and the condition $\mathbf{S}^*\mathbf{S} = \mathbf{I}$ respectively. These two conditions in the lossless case imply $|R^+| = |R^-|$ and the reciprocity condition $T^+ = T^- \equiv T$ in addition of the energy conservation. Therefore, the scattering matrix of a lossless time-reversible system has always the same form, regardless of the physical nature of the involved wave fields and the complexity of the analyzed structure. The general relationships of the S-matrix of fields containing evanescent components have been derived in several works [64–66], showing that the reciprocity condition is independent of the presence of the evanescent modes.

### *13.2.2 Non-mirror Symmetric Systems*

A non-mirror symmetric system, having different scattering properties from each side, presents $R^+ \neq R^-$ and $T^+ = T^- = T$ for a reciprocal scattering problem. The eigenvalues of the S-matrix are expressed as

$$\lambda_{1,2} = T \pm [R^- R^+]^{1/2}, \tag{13.2}$$

and the eigenvectors of the system are

$$\begin{aligned} \mathbf{v_1} &= (v_{11}, v_{12}) = \left(R^+, -\sqrt{R^+R^-}\right), \\ \mathbf{v_2} &= (v_{21}, v_{22}) = \left(\sqrt{R^+R^-}, R^+\right). \end{aligned} \tag{13.3}$$

Therefore, the ratio of the eigenvector components $v_{1i}$ and $v_{2i}$ is $v_{2i}/v_{1i} = (-1)^i (R^-/R^+)^{1/2}$. A zero eigenvalue of the S-matrix corresponds to the case in which the incident waves corresponding to the eigenvectors of the S-matrix can be completely absorbed ($B = C = 0$). This happens when $T = \pm[R^- R^+]^{1/2}$ and the incident waves $A$, $D$ correspond to the relevant eigenvector, giving rise to what is known as *coherent perfect absorption* [67].

### 13.2.3 Mirror Symmetric Systems

A mirror symmetric system produces the same reflection coefficients from both sides, i.e., $R^+ = R^-$, thus implying a symmetric scattering matrix. Therefore, reciprocal and mirror-symmetric one-dimensional (1D) scattering problems are characterized by the following symmetric scattering matrix,

$$S(f) = \begin{pmatrix} T & R \\ R & T \end{pmatrix}, \tag{13.4}$$

where $R$ and $T$ are the complex and frequency dependent reflection and transmission coefficients of the system respectively. The absorption coefficient can thus be defined as $\alpha = 1 - |R|^2 - |T|^2$. The eigenvalues of the scattering matrix are given by

$$\lambda_{1,2} = T \pm R, \tag{13.5}$$

while the eigenvectors are

$$\begin{aligned} \mathbf{v}_1 &= (v_{11}, v_{12}) = (1, +1), \\ \mathbf{v}_2 &= (v_{21}, v_{22}) = (1, -1). \end{aligned} \tag{13.6}$$

Figure 13.2a depicts the scattering problem when a mirror-symmetric system (symmetry with respect to the half plane [white dashed line in Fig. 13.2a]) is excited by a plane wave from the left. First, we consider a Neumann boundary condition $\partial p/\partial x = 0$ imposed at the symmetry plane of the system, i.e., at $x = 0$ where $p$ is the pressure wave solution of the Helmholtz equation (see Fig. 13.2b). The Neumann boundary condition imposes a perfect mirror symmetry creating a virtual image of the

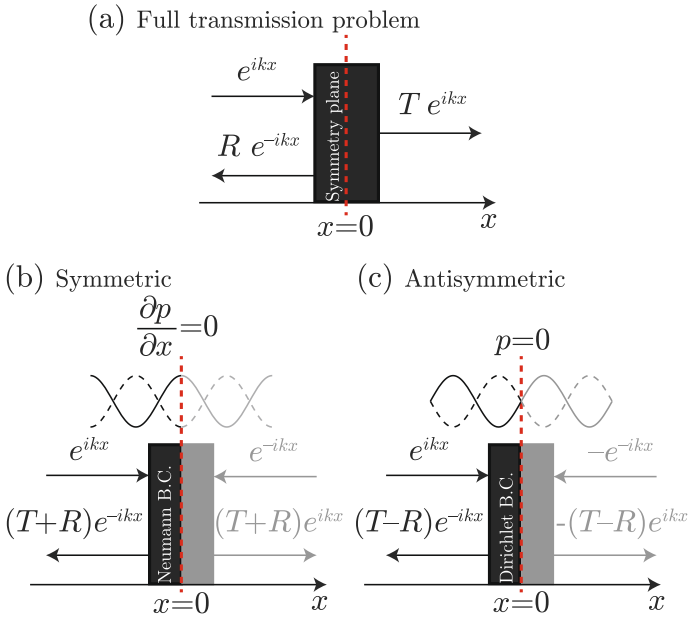



**Fig. 13.2** **a** 1D Transmission problem of a plane wave by a mirror-symmetric resonant scatterer. **b**, **c** Show the reflection problem produced when a Neumann and a Dirichlet boundary conditions are respectively considered in the symmetry plane of the symmetric resonant scatterer (red dashed lines in (**b**) and (**c**)). Continuous line represents the incident pressure wave and dashed line represents the reflected wave due to the boundary condition. In gray, we show the image generated by the presence of the boundary condition. Figure adapted with permission from [61]

full problem on the right side. Therefore, the reflection coefficient of this particular subproblem, $R_s$, can be calculated from the reflection and transmission coefficients of the initial transmission problem, $R_s = R + T$. The subindex $s$ means symmetric since the Neumann boundary condition selects only modes that are symmetric with respect to the symmetry plane where the condition is imposed. Second, we consider a Dirichlet boundary condition, $p = 0$, imposed at the mirror-symmetry plane of the system, i.e., at $x = 0$ (see Fig. 13.2c). This plane acts as a mirror creating a virtual image on the acoustic field, but introducing on it a phase shift of $\pi$. The reflection coefficient of this particular subproblem, $R_a$, can be calculated from the reflection and transmission coefficients of the initial transmission problem, $R_a = R - T$. The subindex $a$ means antisymmetric since the Dirichlet boundary condition imposes only antisymmetric modes with respect to the symmetry plane. Note that the two eigenvalues of the scattering matrix of the original problem, $\lambda_1$ and $-\lambda_2$, correspond to the reflection coefficients of the reflection subproblems with Neumann and Dirichlet conditions, respectively. In other words, the original transmission problem can be decomposed in a symmetric reflection problem, $\lambda_1 = R_s$, and an antisymmetric reflection problem, $\lambda_2 = -R_a$. Thus, the original scattering coefficients read as

$$R = \frac{R_s + R_a}{2}, \quad T = \frac{R_s - R_a}{2}, \quad \alpha = \frac{\alpha_s + \alpha_a}{2}, \tag{13.7}$$

where $\alpha_s = 1 - |R_s|^2$ and $\alpha_a = 1 - |R_a|^2$ are the absorption coefficients of the reflection subproblems with Neumann and Dirichlet boundary conditions respectively. Achieving $\alpha = 1$ implies that the reflection coefficients of the two subproblems vanish at the same frequency.

#### 13.2.3.1 Point Symmetric Resonators

We now further consider punctual scatterers, i.e., their size is infinitesimal. In other words, the wavelength corresponding to the working frequency is much larger than the size of the resonators. This case is relevant to the study the absorption by deep sub-wavelength scatterers. Imposing the continuity of the wave-field at this point [52] yields $1 + R = T$. This corresponds to $R_a = -1$, i.e., the scatterer is transparent to antisymmetric incident waves, $\alpha_a = 0$, and thus $\alpha = \alpha_s/2 \leq 1/2$. The maximum value of one-sided absorption appearing at $f_{\max}$ is $\alpha(f_{\max}) = 1/2$. It corresponds to $\alpha_s(f_{\max}) = 1$ which gives $R_s(f_{\max}) = \lambda_1(f_{\max}) = 0$, and $T(f_{\max}) = -R(f_{\max}) = 1/2$. Thus, the condition $\alpha(f_{\max}) = 1/2$ corresponds to CPA in the two-incident wave problem for symmetric and in-phase incoming waves at $f_{\max}$, i.e., $v_2(f_{\max})/v_1(f_{\max}) = 1$ [68].[1]

#### 13.2.3.2 Point Symmetric Degenerate Resonators

Perfect absorption in one-dimensional (1D) reciprocal problems with one-side excitation appears when the two eigenvalues of the scattering matrix vanish at the same frequency [49, 52]. By inspection of (Eq. 13.7), perfect absorption in mirror-symmetric 1D reciprocal problems can only be achieved when the symmetric and the antisymmetric reflection problems vanish at the same frequency. In this case, $\alpha_s = \alpha_a = 1$ and thus $\alpha = 1$. This means that we need degenerate resonances to perfectly absorb waves, i.e., resonators with both symmetric and antisymmetric resonances at the same frequency. Note that, if only symmetric or antisymmetric resonances are excited, as shown in the previous section for point symmetric resonators, only half of the problem can be impedance matched and thus the maximal absorption[2] that could be reached is $\alpha = 0.5$.

---

[1] The same reasoning can be conducted when considering continuity of velocity. This implies $1 - R = T$. This corresponds to $R_s = 1$, i.e., the scatterer is transparent to symmetric incident waves, $\alpha_s = 0$, and thus $\alpha = \alpha_a/2 \leq 1/2$. The maximum value of one-sided absorption at $f_{\max}$ is $\alpha(f_{\max}) = 1/2$. It corresponds to $\alpha_a(f_{\max}) = 1$ which gives $R_a(f_{\max}) = -\lambda_2(f_{\max}) = 0$, and $T(f_{\max}) = R(f_{\max}) = 1/2$. Thus, the condition $\alpha(f_{\max}) = 1/2$ corresponds to CPA to the two-incident waves problem for antisymmetric and in phase incoming wave at $f_{\max}$, i.e., $v_2(f_{\max})/v_1(f_{\max}) = 1$

[2] In real systems the absorption can be greater than this value because some overlapping occurs due to the bandwidth of the symmetric and antisymmetric modes. This is the case of porous materials

- In *purely reflection problems* the conditions for perfect absorption can always be obtained. In this case, the scattering matrix and the eigenvalues collapse to the reflection coefficient. The impedance matching conditions or critical coupling conditions produce the perfect absorption [28, 35, 47, 69].
- In *ventilated problems* (i.e. with reflexion and transmission) perfect absorption occurs when the two eigenvalues of the scattering matrix are zero at the same frequency. This condition can only be obtained in some particular cases:
  - In non-mirror symmetric systems unidirectional perfect absorption can be reached.
  - In mirror symmetric systems:
    - Point resonators: Only one type of resonance can be excited, therefore only one of the two sub-problems (symmetric or antisymmetric) can be impedance matched and thus the maximum absorption is $\alpha = 1/2$.
    - Degenerate resonators: Symmetric and antisymmetric resonances can be both excited and impedance matched. In this way the two sub-problems can be critically coupled and perfect absorption can be obtained from both sides of the system.

## 13.3 Interpreting the Perfect Absorption: Complex Frequency Plane and Argand Diagram

The scattering coefficients, i.e., the reflection and transmission coefficients, are complex quantities depending on the frequency. Therefore, the eigenvalues, being linear combinations of the scattering coefficients, are also complex and frequency dependent parameters. Regardless the symmetry of the resonator, the condition of perfect absorption at a given frequency, $\omega_{PA}$, is obtained when the two eigenvalues of the scattering matrix are zero at this frequency. In this section, we introduce two techniques to interpret and visualize the perfect absorption condition.

because they usually show a good impedance matching. Therefore, symmetric and antisymmetric modes can overlap even when these resonances appear at different frequencies.

### 13.3.1 Complex Frequency Plane

The first method consists in evaluating the eigenvalues of the scattering matrix in the complex frequency plane. We define the angular frequency as a complex number, $\omega_C = \omega_R + i\omega_I$. Notice that $\omega_R$ represents the observable values of the angular frequency in classical harmonic regime (while $\omega_I$ is related to energy loss and gain). Due to the time invariant symmetry of the scattering matrix (here we consider only linear problems), the $S$-matrix satisfies the following relation $\overline{S(\overline{\omega})} = S^{-1}(\omega)$ where $\overline{S(\omega)}$ and $\overline{\omega}$ represent the complex conjugate of $S(\omega)$ and $\omega$, respectively [35]. This implies that if the eigenvalues of the S-matrix have pairs of poles and zeros, first they appear by pairs, and second, they are complex conjugates in the lossless case [35, 70]. These properties are general [71]; they come from the structure of the wave equation (Helmholtz equation) and are independent of the one-mode approximation. Without loss of generality, we can evaluate the eigenvalues in the complex frequency plane, i.e., $\lambda_{1,2} = \lambda_{1,2}(\omega_C)$ (see Fig. 13.3a, b) for two examples of representation). When losses are introduced, the zero/pole pair moves. The perfect absorption will only appear when the zero of both eigenvalues appears at the same position on the real frequency axis. Thus, by tracking the trajectories of the zeros of the eigenvalues of the S-matrix in the complex frequency plane, the configurations for perfect absorption can be identified.

Two important properties of the scattering matrix [70]:

- Let us consider the case in which $\omega \in \mathbb{R}$. In this case, $\overline{R(\omega)} = R(-\omega)$ and $\overline{T(\omega)} = T(-\omega)$, therefore $\overline{S(\omega)} = S(-\omega)$, which by time reversal symmetry implies, $S(-\omega) = S^{-1}(\omega)$.
- Let us consider the case in which $\omega \in \mathbb{C}$. In this case, $\overline{R(\omega)} = R(-\overline{\omega})$ and $\overline{T(\omega)} = T(-\overline{\omega})$. Then, $\overline{R(\overline{\omega})} = R(-\omega)$ and $\overline{T(\overline{\omega})} = T(-\omega)$. Therefore, $\overline{S(\overline{\omega})} = S(-\omega)$, which by time reversal symmetry implies, $\overline{S(\overline{\omega})} = S^{-1}(\omega)$.

Several properties can be described by interpreting the eigenvalue problem in the complex frequency plane. Let us consider for simplicity a purely reflection problem. In this case, the scattering matrix and the eigenvalues collapse to the reflection coefficient. Due to the properties previously discussed, the reflection coefficient has pairs of zeros and poles that are complex conjugates of each other for the lossless case. With the $e^{-\imath\omega t}$ sign convention, the zeros are located in the positive imaginary plane. The imaginary part of the complex frequency of the poles of the reflection coefficient represents the energy leakage of the system into the free space [35]. Once the intrinsic losses are introduced in the system, the zeros of the reflection coefficient move downwards to the real frequency axis. For a given frequency, if the intrinsic losses perfectly balance the energy leakage of the system, a zero of the reflection coefficient can be exactly located on the real frequency axis and therefore perfect absorption is obtained. This condition is also known as critical coupling [28].

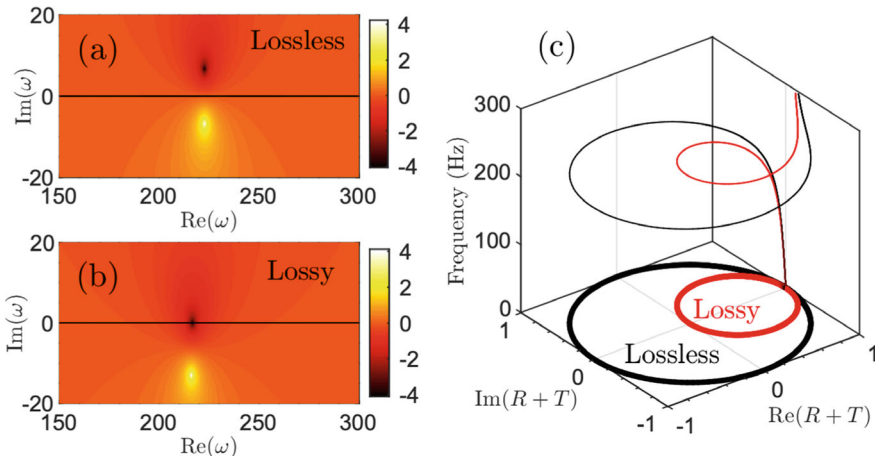



**Fig. 13.3** **a**, **b** Show two examples of representation in the complex frequency plane. **a** In the lossless case in which the pole (yellow) and zero (black) are complex conjugates. **b** Shows the lossy case for the case in which the zero is placed on the real frequency axis. **c** Represents the evolution of the real and imaginary parts of $R + T$ for a given system in the lossless and lossy cases. The projection in the complex plane represents the Argand diagram

The complex frequency plane allows us:

- to visualize the perfect absorption condition when both eigenvalues have the zero on the real frequency axis and at the same frequency,
- to evaluate the losses of the system. If the zero of the eigenvalues is in the positive imaginary part (with $e^{-i\omega t}$ sign convention), additional losses should be introduced in the system to fulfill the perfect absorption condition. However, if the zero is in the negative imaginary part, the system has too much losses to fulfill the perfect absorption condition.

### *13.3.2 Argand Diagram*

Some times the scattering coefficients cannot be evaluated in the complex frequency plane. It is the case, for example, in an experimental evaluation of them. In this case, we can use another technique to both interpret and visualize the perfect absorption condition.

The representation in the complex plane of the eigenvalues of the scattering matrix, i.e., their real part ($x$-axis) in terms of the imaginary part ($y$-axis) for each frequency ($z$-axis) can help to understand the perfect absorption condition. The representation of a complex number in the complex plane is known as the Argand diagram or

Nyquist plot in electronic engineering and signal processing (see Fig. 13.3c for an example of representation). In what follows, we represent the projection of either the scattering coefficients or the eigenvalues of the scattering matrix in the complex plane for each real frequency. In this representation, the perfect absorption condition will be met when the two eigenvalues cross the origin of coordinates, i.e., when their real and imaginary parts are zero at the same frequency.

In the lossless case, the projections are circumferences of unitary radii, centered at the origin of coordinates. As soon as losses are introduced, the radius of the circumference reduces and the center of it changes its position. Until the origin of the complex plane is encapsulated in the circumference, perfect absorption is not reached and additional losses should be introduced. However, if the origin of coordinates is outside the circumference, the system has too much losses and the perfect absorption cannot be fulfilled unless losses are removed, which usually is not possible [44].

The Argand diagram of the eigenvalues of the scattering matrix allows us:
- to visualize the perfect absorption condition when both eigenvalues cross the origin of coordinates at the same frequency in the complex plane,
- to evaluate the amount of losses of the system. If the origin of coordinates is encapsulated by the circumference surface, the system presents weak losses, while if the origin stands outside, the system is too lossy to produce perfect absorption.

## 13.4 Acoustic Metamaterials Made of Helmholtz Resonators for Perfect Absorption in Ventilated Problems

### *13.4.1 Sub-Wavelength Systems with Slow Waves*

We consider a 2D flat panel composed of a periodic distribution of slits of width $h$ separated a distance $d$ and distributed in the $x_1$ direction as shown in Fig. 13.4. Each slit is loaded by $M$ Helmholtz resonators (HRs) periodically separated by a distance $a$ (lattice constant). The HRs considered in this work can be either 2D, made of combination of slits that form the neck and cavity of length and width $l_n$ and $w_n$, $l_c$ and $w_c$ respectively, or 3D, made of square cross-sectional tubes, with a neck and a cavity widths $w_n$ and $w_c$, and lengths $l_n$ and $l_c$ respectively.

First, we study the dispersion relation of a periodic medium made of the periodic repetition of a unit cell. The unit cell is made of a slit of length $L = Na$ loaded with $N = 1$ HR with resonance frequency $f_{\text{HR}}$. In this case, by applying periodic boundary conditions in a unit cell, we can evaluate the dispersion relation. Figure 13.5a, b show

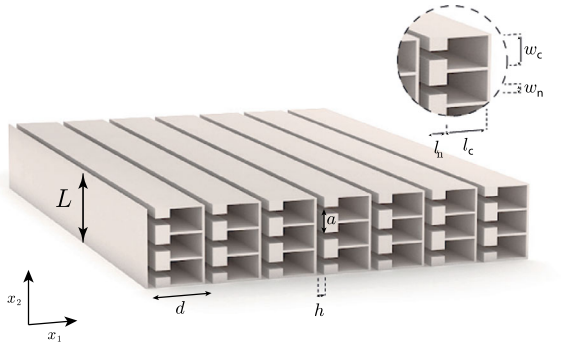



**Fig. 13.4** Conceptual view of the thin panels considered in this chapter. We show an example for a system made of three layers of 2D HRs. The inset shows a conceptual view of a 2D HR

the real and imaginary parts of the dispersion relation.[3] The main feature of this dispersion relation is that a stop band can be observed above the resonant frequency of the HRs. Below the resonance frequency of the HRs a dispersive propagation band is observed, and the wavenumber there is larger than in air. Note also that the maximum value of the wavenumber inside the slit is limited by the discreteness of the system to the value $k_{\max} = \pi N/a$, (see dashed blue curve in Fig. 13.5b). Interestingly, the imaginary part of this dispersion relation in the lossy case becomes important around the resonance frequency. However, the losses are less important when we are far from the resonant frequency of the HRs.

Figure 13.5c shows the real part of the phase velocity in the slit, calculated both in the lossless and lossy cases. Below the resonance frequency of the HRs, slow sound conditions are produced due to the strong dispersion introduced by the resonators. In the lossless case, zero phase velocity can be observed for frequencies right below $f_{\text{HR}}$. In the lossy case, the losses limit the minimum value of group velocity [24, 72], but in our system slow sound velocity can be achieved in the dispersive band below $f_{\text{HR}}$. The average sound speed in the low frequency range is much lower (about 50 m/s) than the speed of sound in air (black dotted line in the main slit).

In order to evaluate how we can slow down the sound velocity to shift the resonance of our system to low frequencies, let us first consider a quarter wavelength resonator of length $L$. We know that the $n$-th resonance of the system is given by the relation $k_{QW}^n = n\pi/4L$. Now, consider that the same quarter wavelength resonator is periodically loaded, with periodicity $a$, by $N = 3$ HRs, i.e., $L = Na$ as shown in the inset of Fig. 13.6. Figure 13.6a shows the dispersion relations of the medium filling the quarter wavelength resonator for the two analyzed cases, i.e., air $k_0 L/\pi$ (black dotted line), and the periodic system made of HRs (red continuous line). It is worth noting here that the resonance condition $k_{QW}^n$ are also plotted. In the quarter wavelength resonator the resonance frequencies will be given by the crossing of these wave numbers with the dispersion relation of air, i.e., the black dotted line $k_0 a/\pi$. However, when the quarter wavelength resonator is loaded by the Helmholtz resonators,

[3] The calculation is done by the Transfer Matrix Method (TMM) for both the lossless and lossy cases. Details of this method are explicitly given in [47].

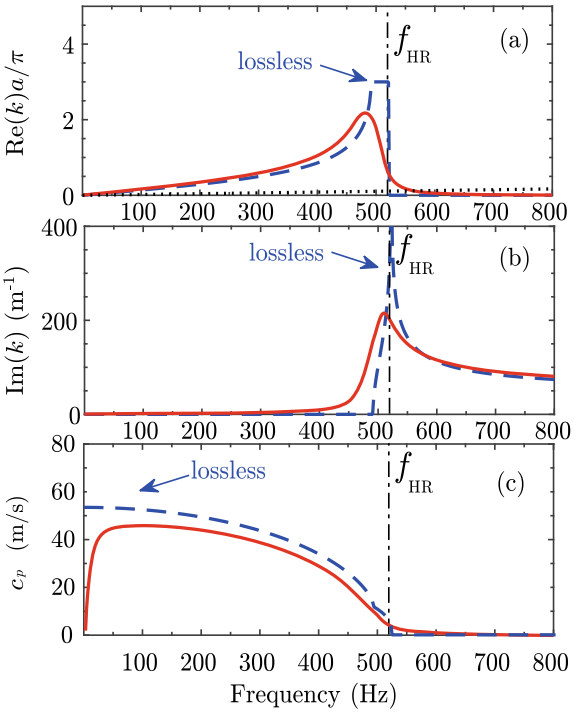



**Fig. 13.5** **a**, **b** Show the real and the imaginary parts of the dispersion relation calculated by the transfer matrix method (TMM) for a metamaterial with parameters $h = 1.2$ mm, $a = 1.2$ cm, $w_n = a/6$, $w_c = a/2$, $d = 7$ cm, $l_n = d/3$, and $l_c = d - h - l_n$. Blue dashed lines represent the lossless case while red continuous lines represent the lossy case. Black dotted line represents the dispersion relation of the main slit without HRs. **c** Phase speed calculated by TMM for the lossless case (dashed blue line) and including thermo-viscous losses (continuous red line). Vertical dash-dotted black line represent the resonant frequency of the HR, $f_{\mathrm{HR}}$

the crossing of these wave numbers with the dispersion relation (red continuous line) appears at much lower frequencies due to the strong dispersion introduced by the HRs. The difference between the resonances of the quarter wavelength resonator and that loaded with HRs is due to the difference in the speed of sound due to the slowing down of the sound velocity.

### *13.4.2 Non-mirror Symmetric Acoustic Metamaterials*

In this section, we analyze the scattering properties of a system made of $N$ detuned HRs loading a waveguide. Due to the detuned HRs, the S-matrix is not symmetric and the scattering properties from both sides of the system must be analyzed.

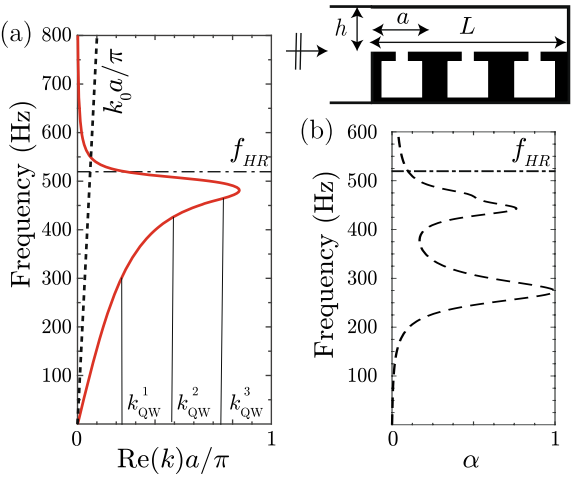



**Fig. 13.6** **a** Real part of the dispersion relation of the resonant periodic system made of the periodic arrangement of resonators (red continuous line). $k^n_{QW}$ shows the wavenumbers of the corresponding $n$ quarter wavelength resonance of a slit of length $L$. Black dotted line shows the dispersion relation of the slit. **b** Upper panel: schematic view of a finite slit of height $h$ and length $L$ loaded by $N = 3$ HRs. Lower panel: absorption coefficient of the system with $N = 3$ HRs

#### 13.4.2.1 Sub-wavelength Non-mirror Symmetric Panel

We start analyzing a system made of $N = 2$ HRs, considering the two directions of incidence, namely *forward* and *backward*, as depicted in Fig. 13.7a, b. The $n$-th resonator of the system presents a resonant frequency at $f_n$. Figure 13.7c–f show the corresponding absorption, reflection and transmission coefficients for each case.[4]

First, in the forward configuration, shown in Fig. 13.7a, $f_1$, a stop band is introduced and the transmission is strongly reduced because the HR acts as a rigidly-backed wall for the right incoming waves above its resonant frequency. Then, the resonator $n = 2$, with $f_2 > f_1$, is tuned to impedance match the system with the exterior medium at frequency $f_{PA}$ between $f_1$ and $f_2$. At this particular frequency, no reflected waves are produced and therefore, $\alpha = 1 - |R^-|^2 - |T|^2 = 1$ holds. As shown in [49] the optimization process looks for the geometry that introduces the exact amount of viscothermal losses to minimize $\varepsilon(f_{PA}) = |R^-(f_{PA})|^2 + |T(f_{PA})|^2$, i.e., maximizing the absorption of energy at $f_{PA}$. In this situation, unidirectional perfect absorption is observed. The optimization of the geometry of the system, shows that a deep sub-wavelength panel with a thickness 40 times smaller that the wavelength can be designed [49]. It is worth noting here that the change of

[4] The results are calculated analytically using the transfer matrix method (TMM) in which the thermoviscous losses are accounted for, numerically using finite element method (FEM) and experimentally validated using stereo-lithographic 3D printed structures and impedance tube measurements. Details can be found in [49].

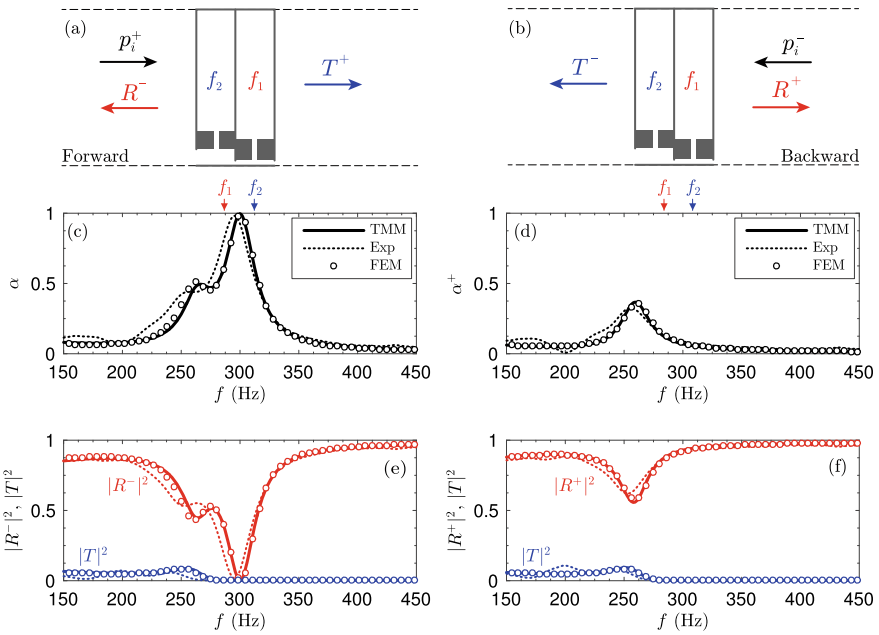



**Fig. 13.7** Scheme of the sub-wavelength non-mirror symmetric panel in (**a**) forward and (**b**) backward configuration. **c** Absorption for the forward configuration obtained using TMM (continuous line), FEM (circles), and experiment (dotted line). **e** Corresponding reflection and transmission coefficients. **d** Absorption for the backward configuration. **f** Corresponding reflection and transmission coefficients. The arrows mark the resonance frequencies of the HRs, $f_1$ and $f_2$. Figure adapted with permission from [49]

section in the main waveguide helps to achieve the impedance matching, specially for very thin systems as the one presented here.

Second, in the backward propagation also shown in Fig. 13.7b, the wave impinges first the lowest resonance frequency resonator from the right, $f_1$. Now, almost no transmission is allowed in the waveguide at this frequency. As the waveguide is not impedance matched at $f_1$ in backward direction, reflection is high and absorption is poor ($\alpha^+ = 0.05$). For frequencies below $f_2$, propagation is allowed in the main waveguide and the effect of the second HR may be visible inducing a decrease of the reflection coefficient. However, the impedance matching in the backward direction is not achieved and only a low absorption is observed near the resonance frequency of the first resonator.

In order to go further in the physical understanding of the scattering problem, we analyze the eigenvalues and eigenvectors of the S-matrix in the complex frequency plane. Let us start by considering the lossless case, neglecting the thermo-viscous losses. The eigenvalues shown in Fig. 13.8a, b present pairs of zeros and poles, each pole identified with a resonance of the system. As previously discussed in Sect. 13.2, each pole presents a zero that is its complex conjugate in the lossless case [35].

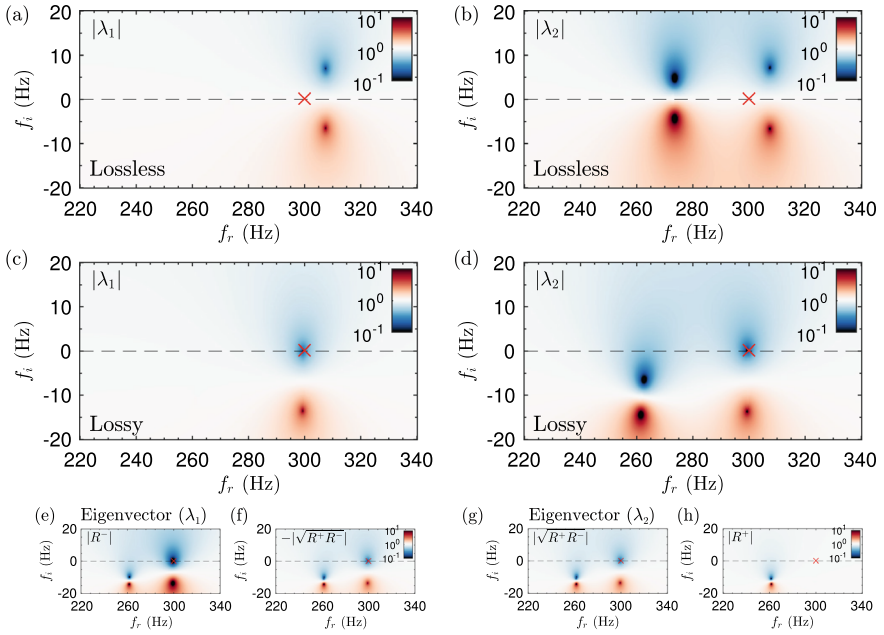



**Fig. 13.8** Complex frequency representation of the two eigenvalues of the scattering matrix, $|\lambda_1|$, $|\lambda_2|$, **a**, **b** in the lossless case and **c**, **d** including the thermo-viscous losses in the resonators and the main waveguides. Colormap in $10\log_{10}|\lambda_i|^2$, $i = 1, 2$, scale. Figure adapted with permission from [49]

Now, we account for the visco-thermal losses in the resonators and the waveguides. In general, once losses are introduced the zero-pole structure of a given system moves in the complex plane, and the zeros get closer to the real frequency axis. Figure 13.8c, d show the eigenvalues of the S-matrix when the thermo-viscous losses are introduced. At the frequency $f_{PA}$, both eigenvalues, $\lambda_{1,2}$, given by (13.2), present a zero exactly located at the real axis. This implies $T = \sqrt{R^+R^-}$, and as the system is tuned to present $R^- = 0$, then $T = \sqrt{R^+R^-} = 0$ and as a consequence $\lambda_{1,2}(f_{PA}) = 0$. This implies perfect absorption at $f_{PA}$.

However, the information provided by the eigenvalues is not sufficient to determine from which side the perfect absorption is produced. In order to draw the complete picture of the physical process, the corresponding eigenvectors are analyzed. Figure 13.8e–h show the eigenvectors corresponding to $\lambda_1$ and $\lambda_2$, given by (13.3), respectively. We can see that $R^- = 0$, while $R^+ \neq 0$ at $f_{PA}$. This implies that the structure is only impedance matched to the surrounding medium when the incoming wave impinges the system from the forward direction. Therefore, unidirectional perfect absorption is observed.

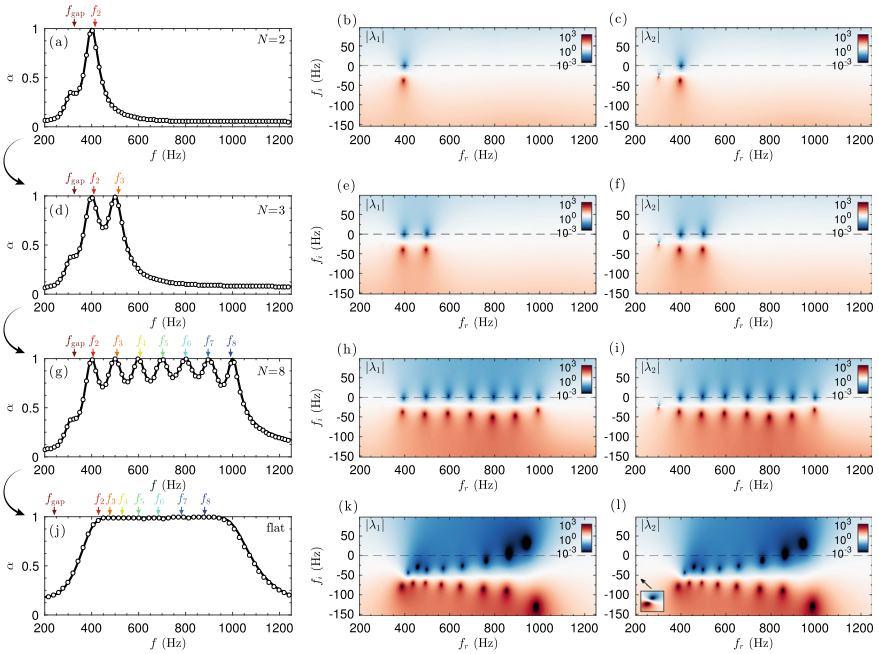



**Fig. 13.9** Process to critically couple the rainbow-trapping absorbers. **a** Absorption using $N = 2$ HRs obtained using TMM (continuous lines) and FEM simulations (markers), **b**, **c** corresponding complex frequency plane representation of the eigenvalues of the scattering matrix. **d** Absorption using $N = 3$ HRs and **e**, **f** corresponding complex frequency plane. **g** Absorption using $N = 8$ HRs and **h**, **i** complex frequency plane. **j** Optimized broadband and flat absorption using $N = 8$ HRs, **k**, **l** corresponding complex frequency plane. Figure adapted with permission from [49]

### 13.4.2.2 Rainbow-Trapping Absorber

The concept described in the previous section can be applied to design broadband perfect absorbers, i.e., to extend the absorbing performance in a wide frequency range. The idea is to create a frequency-cascade of stop band and critically coupled resonators in order to generate a rainbow-trapping effect. The process is as follows. First, we tune the deepest resonator ($n = 1$) in the waveguide to reduce the transmission above a frequency $f_1$. Second, in the same way as previously done, a second resonator with slightly higher resonance frequency, $f_2$, is placed in the preceding segment of the waveguide. Both the geometry of this resonator and the section of the waveguide have to be tuned to impedance match the system at a frequency $f_1^{PA}$ between $f_1$ and $f_2$. Therefore, perfect absorption is fulfilled when the system is excited from one side. Figure 13.9a–c depicts the process for these 2 resonators. Figure 13.9a shows a peak of perfect absorption and, as shown in Fig. 13.9b, c, both eigenvalues of the scattering matrix present a zero at the same real frequency. Note this latter HR also reduces the transmission at higher frequencies. Then, the process

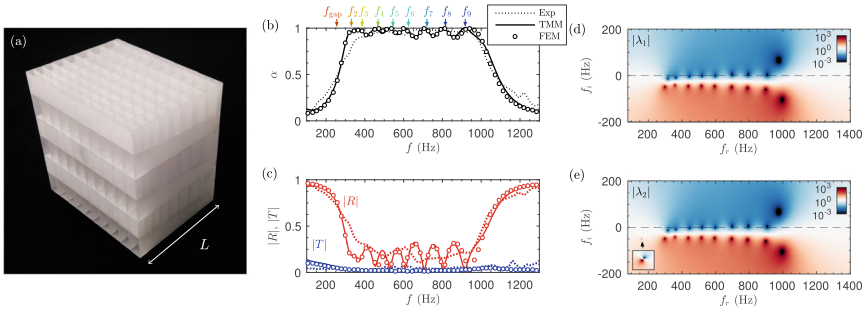



**Fig. 13.10** **a** Photograph of the sample containing $10 \times 3$ unit cells. **b** Absorption obtained by using the TMM (continuous line), FEM simulations (circles) and measured experimentally (dotted line). **c** Corresponding reflection (red curves) and transmission (blue curves) coefficients in amplitude. **d**, **e** Complex frequency representation of the eigenvalues of the scattering matrix, $\lambda_{1,2}$. Colormap in $10 \log_{10} |\lambda|^2$ scale. Figure adapted with permission from [49]

can be repeated by extending the waveguide with more segments, each one with a tuned HR the resonance frequency f which is higher than that of the preceding one. Another HR is added with a slightly higher resonance frequency, $f_3$. The system is again tuned, but this time looking for perfect absorption at two single frequencies, $f_{1,PA}$ and $f_{1,PA}$, with $f_2 < f_{2,PA} < f_3$. Figure 13.9d shows the obtained absorption coefficients where two peaks of perfect absorption are observed, as demonstrated also by the location of the zeros of the eigenvalues of the scattering matrix on the real frequency axis, shown in Fig. 13.9e, f.

This process is iteratively repeated until $N = 8$ HRs were included. Figure 13.9h–i show the $N - 1$ peaks of perfect absorption and the corresponding complex frequency plane representation of the eigenvalues of the scattering matrix, respectively. Note that strictly speaking perfect absorption can only be achieved at $N - 1$ singular frequencies, $f_{PA}^n$, due to frequency cascade effect. However, flatter absorption can be generated due to the overlapping of the zeros of $\lambda_{1,2}$ if the quality factor of the resonances is reduced. This can be achieved by tuning again the geometrical parameters of the system, using as the initial condition to the optimization algorithm the previous geometry, and using a cost function covering a broad frequency band as $\varepsilon_{\text{RTA}} = \int_{f_1}^{f_N} (|R^-|^2 + |T|^2) df$. The final, broadband, and quasi-perfect absorption is shown in Fig. 13.9j. It is worth noting here that using a wide-bandwidth cost function does not ensure that all the resonances remain critically coupled, as it is shown in the complex frequency plane representation of the eigenvalues of the scattering matrix in Fig. 13.9k, l. However, the ripples in the absorption can be strongly reduced and the total absorption of energy in a frequency band can be maximized.

By using the previous methodology, we have designed a rainbow-trapping absorber (RTA) using $N = 8$ HRs. The dimensions of all the geometrical elements that compose the structure were quantized to the 3D printing resolution. Manufacturing details are given in [49]. The manufactured sample is shown in Fig. 13.10a.

Figure 13.10b, c show the absorption, reflection, and transmission of the device.[5] The deepest resonator ($n = 1$) presents a resonance frequency of $f_1 = f_{\text{gap}} = 259$ Hz, causing the transmission to drop. The resonators were tuned following the process previously described, with increasing resonance frequencies ranging from 330 to 917 Hz. As a result of the frequency-cascade process, the impedance of the structure in the working frequency range is matched with the exterior medium while the transmission vanishes. As a consequence, the RTA presents a flat and quasi-perfect absorption coefficient over this frequency range (see Fig. 13.10b). It can be observed that at low frequencies small differences between the measurements and the models are noticed. These disagreements are mainly caused by imperfections in the sample manufacturing, by imperfect fitting of the structure to the impedance tube, by the possible evanescent coupling between adjacent waveguides and adjacent HRs, and/or by the limitations of the visco-thermal model used at the junctions between waveguide sections.

The corresponding representation of the two eigenvalues of the S-matrix in the complex frequency plane is shown in Fig. 13.10d, e. We can see that even under the constraints imposed by the manufacturing process, all the $N - 1$ zeros of the eigenvalues that produce the critical coupling of the structure are located very close to the real frequency axis being the zeros of $\lambda_1$ at the same frequencies as those of $\lambda_2$. Note that not all the zeros are located exactly on the real axis in the manufactured system, but the quality factor of the resonances is very low, therefore they overlap producing quasi-perfect sound absorption over a frequency band ranging from 300 to 1000 Hz for a panel 10 times thinner than the wavelength at 300 Hz in air.

For non-mirror symmetric systems unidirectional broadband perfect absorption can be obtained. Three conditions must be simultaneously met:

- The zeros of the eigenvalues of the scattering matrix must be located on the real frequency axis.
- The zeros of both eigenvalues, $\lambda_{1,2}$, must be at same frequency.
- The quality factor of the resonances must be low to overlap in frequency.

These three conditions are mandatory to maximize the broadband absorption of the panels and can be obtained by optimization methods. Perfect absorption may only be obtained at some discrete frequencies, while the broadband character of the absorption is given by low quality factor resonances.

[5] Details of the modeling by the TMM, FEM and also of the experimental set-up are given in [49].

### *13.4.3 Mirror Symmetric Acoustic Metamaterials*

#### 13.4.3.1 Symmetric and Antisymmetric Resonances in Slits Loaded by Helmholtz Resonators

Let us start the discussion by analyzing the scattering coefficients of a system made of a slit loaded by $N$ resonators. This system presents $N$ resonances. For simplicity, but without loss of generality, we analyze here the case with $N = 2$ in which the resonance frequency of the HRs is $f_{HR}$. We analyze the propagation through a slit loaded by two HRs as shown in the inset of the Fig. 13.11a. In this case the scattering coefficients are plotted in Fig. 13.11b, showing two transmission peaks corresponding to the first two Fabry-Perot resonances of the slit. The first two resonances of the slit are clearly visible on Fig. 13.11b, c that depict the absolute value of the total pressure field at these particular frequencies. The first mode is symmetric while the second mode is antisymmetric with respect to the symmetry plane of the system (shown by the dashed line in Fig. 13.11b, c.

Previous discussion allows us to conclude that resonators with symmetric and antisymmetric resonances can be designed with the combination of the discussed systems: a periodic arrangement of two slits loaded respectively by one and two HRs. As a consequence, the resonator design that we propose now, shown in Fig. 13.12, is a combination of slits loaded by one and two resonators. The slit loaded by a single resonator only supports symmetric modes and will thus be named symmetric slit. The slit loaded by two resonators supports both symmetric and antisymmetric modes. It will be mainly used to tune the antisymmetric resonance and will thus be named antisymmetric slit. The geometric parameters of the degenerate resonator, i.e., a resonator with different resonant modes at the same frequency, are defined in Fig. 13.12. The subindex $s$ ($a$) represents the parameters for the symmetric (antisymmetric) slit.

At this stage we have to discuss the unit cell geometry shown in Fig. 13.12. For the experiments, we only have to consider half of it [black areas in Fig. 13.12] as we are using a square impedance tube of side $d_0$. In fact, the walls of the impedance tube act as mirrors generating the virtual images (gray areas in Fig. 13.12) with respect to the position of the rigid wall in the tube, i.e., the dot-dashed line in Fig. 13.12.

It is worth noting here that now the resonators are made of two slits that can eventually be coupled through evanescent coupling. Therefore, the modeling with the transfer matrix method, based on plane wave propagation, is not valid anymore. Higher order modes needs to be accounted for in the main waveguides. A multimodal approach needs to be developed. Details of the modeling for this kind of systems are explicitly given in [61]. In particular, we have developed a hybrid model combining both modal decomposition and transfer matrix methods. The modal decomposition of the acoustic field is used in the exterior domains in order to account for the Bloch modes excited at the interfaces of the resonator allowing possibly the evanescent coupling between the different slits. Wave propagation within each slit is modeled by the transfer matrix method as widely done previously because only plane waves are propagating in these slits.

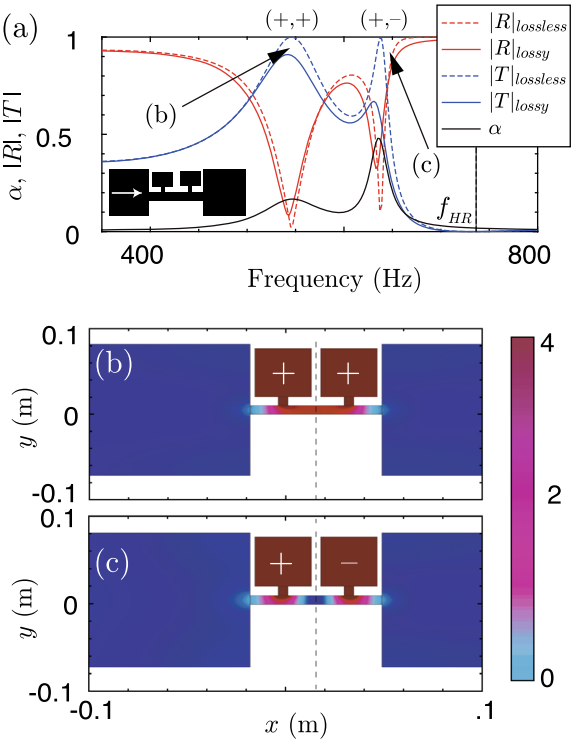



**Fig. 13.11** **a** shows the lossless (dashed lines) and lossy (continuous lines) scattering coefficients for the case of a slit loaded by two identical resonators (red lines correspond to the reflection coefficient while blue lines for the transmission one. Black lines represent the absorption coefficient for the lossy case). Inset shows the schema of the scattering problem, with the incident direction indicated with the withe arrow. Vertical black dashed line shows the symmetry plane of the resonator. **b**, **c** represent the absolute value of the total pressure field for the two first resonances of the slit loaded with two identical resonators. Vertical black dashed line shows the symmetry plane of the resonator. Figure adapted with permission from [61]

#### 13.4.3.2 Antisymmetric Resonator

The antisymmetric slit supports two resonant modes, a symmetric mode and an antisymmetric mode, while the symmetric slit supports a single symmetric mode. Thus, due to the geometry considered in this work only an antisymmetric resonant mode can be excited in the antisymmetric slit. Therefore, we start the discussion with the antisymmetric subproblem. Consider a Dirichlet condition in the mirror-symmetry plane of the degenerate resonator. In the symmetric slit only symmetric modes can be excited. Therefore, no modes will be excited inside this slit when imposing a Dirichlet boundary condition. However, in the antisymmetric slit, only the antisymmetric mode will be excited. Thus, the antisymmetric subproblem can be critically coupled by optimizing only the geometry of the antisymmetric slit. Figure 13.13a, b show the

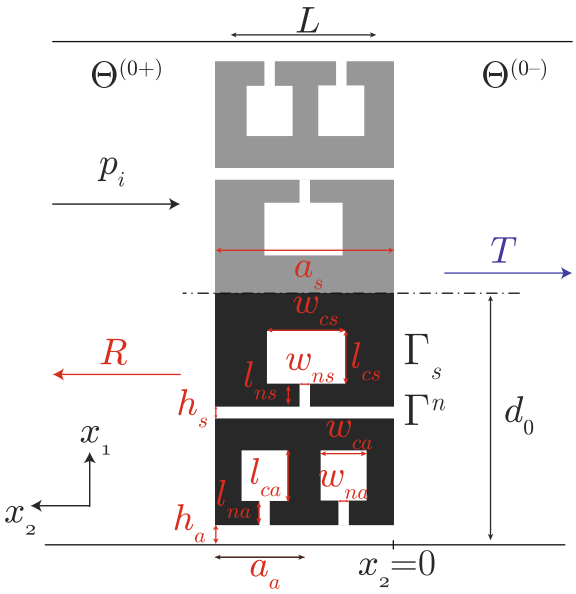



**Fig. 13.12** Scheme of the mirror-symmetric building block used in this work with the definitions of the geometrical parameters. Figure adapted with permission from [61]

absolute value of the total acoustic field of the antisymmetric reflection problem at the frequency presenting perfect absorption. Only the antisymmetric slit is excited. The reflection and absorption coefficients of this problem are shown in Fig. 13.13c. At the target frequency, $f_{PA} = 800$ Hz, perfect absorption is obtained.

#### 13.4.3.3 Symmetric Resonator

Once the antisymmetric subproblem is critically coupled, we have to consider the symmetric problem by imposing a Neumann boundary condition at the mirror-symmetry plane of the degenerate resonator. In that case, symmetric modes exists in both slits. However, as the antisymmetric problem has been critically coupled by optimizing the geometry of the antisymmetric slit, now we only use the geometry of the symmetric slit to critically couple the symmetric subproblem. Figure 13.13d, e show the absolute value of the total acoustic field of the symmetric reflection problem at the frequency with perfect absorption. In this subproblem, the two resonators are excited. The reflection and the absorption coefficients of this subproblem are shown in Fig. 13.13f.

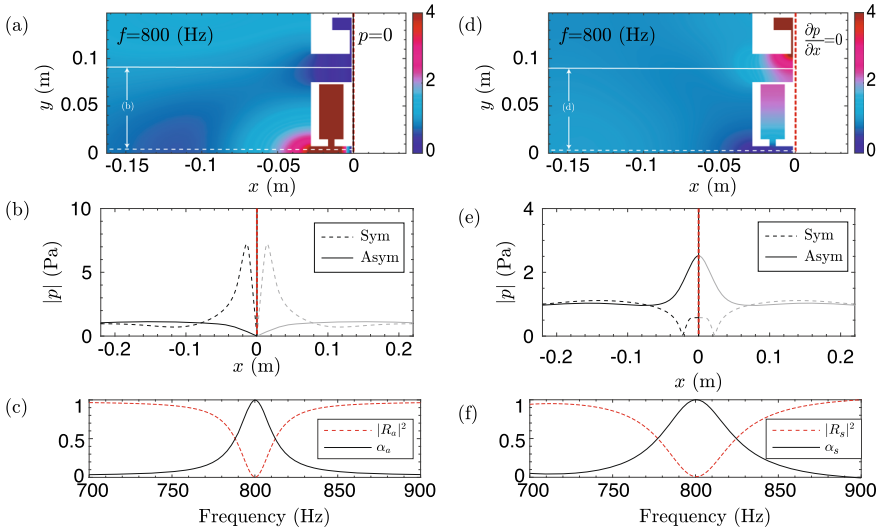



**Fig. 13.13** Critical coupling of the symmetric and antisymmetric problem. **a** Represents the absolute value of the total acoustic pressure field at the perfect absorption of the antisymmetric problem. **b** Shows the absolute value of the total pressure field, $|p|$, along the profiles shown in (**a**) considering the field in each slit for the antisymmetric problem. **c** Shows the reflection and the absorption coefficient of the antisymmetric problem. **d** Represents the absolute value of the total acoustic pressure field at the perfect absorption of the symmetric problem. (e) Shows the absolute value of the total acoustic field, $|p|$, along the profiles shown in (c) considering the field in each slit for the symmetric problem. (f) Shows the reflection and the absorption coefficient of the symmetric problem. Figure adapted with permission from [61]

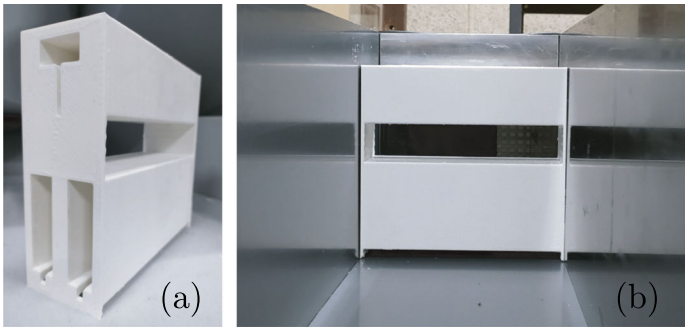



**Fig. 13.14** **a** Picture of the 3D printed symmetric resonant scatterer. **b** Picture of the symmetric resonant scatterer inside the impedance tube. Figure adapted with permission from [61]

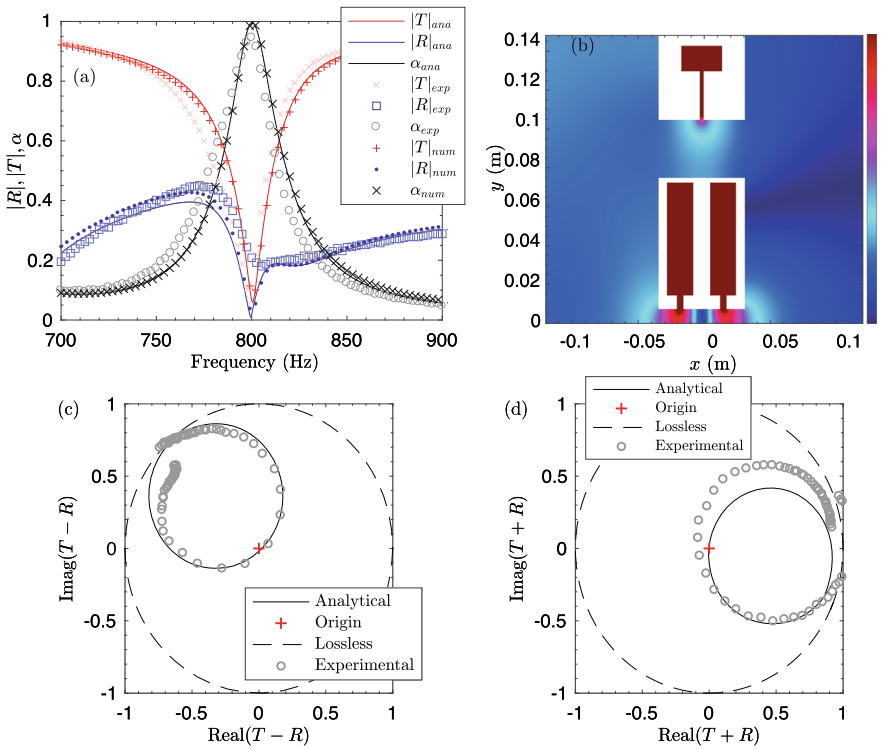



**Fig. 13.15** **a** Analytical, numerical and experimental scattering coefficients of the full problem. **b** Represents the absolute value distribution of the acoustic field at the perfect absorption of the full scattering problem. **c**, **d** Show the Argand diagram of the two eigenvalues of the scattering matrix $T \pm R$ respectively. The diagram for the lossless case is plotted with dashed lines. The diagram for the lossy case is represented with continuous black line as analytically obtained and with open gray circles from the experimental results. The red cross shows the origin of coordinates. Figure adapted with permission from [61]

#### 13.4.3.4 Perfect Absorption in Mirror Symmetric Systems

In the previous subsection, we have critically coupled the symmetric and the antisymmetric reflection subproblems. This means that the two eigenvalues of the scattering matrix vanish at the same frequency in the full transmission problem with the optimized geometry. Therefore, the full problem is critically coupled and perfect absorption is expected. Details of the geometry obtained from the optimization problem for the complete resonator can be found in [61]. A picture of the 3D printed the resonator is shown in Fig. 13.14b. The resonator is mounted in the square cross-sectional impedance tube (Fig. 13.14c) and the scattering parameters of the full problem are measured. It is worth noting here that the lateral walls of the structure have been filled with vaseline to avoid the leakage at the lateral interfaces and force the sound to propagate only in the slits.

Figure 13.15a shows the scattering coefficients of the full transmission problem. The agreement between the model, the numerical simulations, and the experimental results is very good. Note that the presence of the Bloch waves is crucial in this kind of systems: if only plane waves had been accounted for in the system, the model would not have reproduced the whole wave process because the evanescent coupling would have been neglected (see [61] and its supplementary material for more details). When the Bloch waves are considered, a perfect absorption peak appears at $f_{PA} = 800$ Hz as analytically, numerically, and experimentally observed. Figure 13.15b shows the acoustic field of the full problem at the perfect absorption peak. It is worth noting here that perfect absorption is very sensible to the geometry of the resonators and this explains the slight discrepancies between the analytical or numerical predictions and the experimental results. The symmetric slit exhibits the symmetric Fabry-Perot mode while the antisymmetric slit exhibits the antisymmetric Fabry-Perot mode. Both modes are excited at the same frequency, i.e., the structure presents a degenerate resonance.

In order to interpret the perfect absorption condition, we have analyzed the Argand diagram of the eigenvalues of the scattering matrix. Figure 13.15c, d show the Argand diagram for these quantities. Each point of these diagrams corresponds to a frequency, i.e., we project every frequency in the complex plane. Black dashed line shows the Argand diagram in the lossless case, i.e., the case in which the circumference has a unity radius for the two eigenvalues and is centered in the origin of coordinates of the complex plane. As soon as losses are considered, the radius of the circumference is reduced and its center moves in the complex plane. Black continuous line and open circles represent the theoretical and experimental Argand diagrams respectively. We notice that the trajectory of the Argand diagram crosses the origin of coordinates for the two eigenvalues, the crossing appearing at the same frequency, $f_{PA}$, for both eigenvalues.

To obtain broadband and perfect absorption in the transmission problem with mirror-symmetric systems, both the symmetric and anti-symmetric sub-problems must be impedance matched simultaneously at the same frequency. This can only be done by using degenerate resonators with symmetric and antisymmetric resonances. The impedance match of each problem at the same frequency implies that the two eigenvalues of the scattering matrix will vanish at the same frequency. As the scattering matrix in this case is symmetric the system presents perfect absorption at the target frequency for the two different incidence sides. This is in clear opposition to the non-mirror symmetric systems in which unidirectional perfect absorption can be obtained. In terms of Argand diagrams, this means that the trajectories of the two eigenvalues on the complex plane cross the origin of coordinates at the same frequency.

## 13.5 Conclusions

The conditions to obtain perfect absorption in ventilated problems with both mirror and non-mirror symmetric systems are discussed in this chapter. We have shown that with non-mirror symmetric systems unidirectional perfect absorption can be obtained. In the case of mirror-symmetric system, perfect absorption can be obtained by means of degenerate resonators, i.e., resonators presenting symmetric and anti-symmetric resonances impedance matched at the same frequencies. Two examples of acoustic metamaterials made of Helmholtz resonators are described, showing the possibilities of both non-mirror and mirror symmetric systems. These materials are based on the concept of slow waves allowing to shift the resonances to the deep sub-wavelength regimes. Two different techniques to interpret and visualize the perfect absorption conditions are described in detail in the chapter: the representation of the eigenvalues of the scattering matrix (or the scattering parameters) in the complex frequency plane, and in Argand diagrams. The two techniques are illustrated by examples, providing a deep insight on the conditions to obtain perfect sound absorption in acoustic metamaterials.

The results presented in this chapter show the advances in the field of deep sub-wavelength absorption in the ventilated problems for airborne acoustics. Recent works have also shown that lossy symmetric periodic structures, as sonic crystals made of porous scatterers can exhibit quasi-perfect absorption at higher frequencies because Fabry-Perot interferences usually coallesce around the frequency of symmetry band inversion for two and three-dimensional structures [73]. This chapter and the novel results in the field could motivate new developments to design broadband and omnidirectional deep sub-wavelength acoustic absorbers that have the potential to transform the traditional noise control methods.

**Acknowledgements** Authors want to acknowledge Antonio A. Fernández-Marín, G. Theocharis and O. Richoux for the discussions on the topics related with the topic of the current chapter. The authors gratefully acknowledge the ANR-RGC METARoom (ANR-18-CE08-0021) project, the project HYPERMETA funded under the program Étoiles Montantes of the Région Pays de la Loire. This article is based upon work from COST Action DENORMS CA15125, supported by COST (European Cooperation in Science and Technology). N.J. acknowledges financial support from "Juan de la Cierva-Incorporación" grant IJC2018-037897-I funded by MCIN/AEI/ 10.13039/501100011033.

## References

1. D.G. Baranov, A. Krasnok, T. Shegai, A. Alù, Y. Chong, Coherent perfect absorbers: linear control of light with light. Nat. Rev. Mater. **2**(12), 17064 (2017)
2. V. Romero-García, N. Jiménez, G. Theocharis, V. Achilleos, A. Merkel, O. Richoux, V. Tournat, J.-P. Groby, V. Pagneux, Design of acoustic metamaterials made of Helmholtz resonators for perfect absorption by using the complex frequency plane. Comptes Rendus. Physique **21**(7–8), 713–749 (2020)

3. F. Lemoult, N. Kaina, M. Fink, G. Lerosey, Wave propagation control at the deep subwavelength scale in metamaterials. Nat. Phys. **9**(1), 55–60 (2013)
4. N. Engheta, R.W. Ziolkowski, *Metamaterials: Physics and Engineering Explorations* (Wiley, 2006)
5. V. Romero-García, A. Hladky-Hennion, *Fundamentals and Applications of Acoustic Metamaterials: From Seismic to Radio Frequency* (ISTE Willey, 2019)
6. P. Deymier (ed.), *Acoustic Metamaterials and Phononic Crystals* (Springer, Berlin, Heidelberg, 2013)
7. R. Craster, S. Guenneau, *Acoustic Metamaterials, vol. 166 of Springer Series in Materials Science* (Spinger, 2013)
8. X. Yu, J. Zhou, H. Liang, Z. Jiang, L. Wu, Mechanical metamaterials associated with stiffness, rigidity and compressibility: a brief review. Progr. Mater. Sci. **94**, 114–173 (2018)
9. D. Mu, H. Shu, L. Zhao, S. An, A review of research on seismic metamaterials. Adv. Eng. Mater. **22**(4), 1901148 (2020)
10. Z. Liu, X. Zhang, Y. Mao, Y.Y. Zhu, Z. Yang, C.T. Chan, P. Sheng, Locally resonant sonic materials. Science **289**(5485), 1734–1736 (2000)
11. S.H. Lee, C.M. Park, Y.M. Seo, Z.G. Wang, C.K. Kim, Composite acoustic medium with simultaneously negative density and modulus. Phys. Rev. Lett. **104**, 054301 (2010)
12. C.E. Bradley, Acoustic Bloch wave propagation in a periodic waveguide, *Technical Report of Applied Research Laboratories, Report No. ARL-TR-91-19 (July)* (The University of Texas at Austin, 1991)
13. N. Sugimoto, T. Horioka, Dispersion characteristics of sound waves in a tunnel with an array of Helmholtz resonators. J. Acoust. Soc. Am. **97**, 1446 (1995)
14. N. Fang, D. Xi, J. Xu, M. Ambati, W. Srituravanich, C. Sun, X. Zhang, Ultrasonic metamaterials with negative modulus. Nat. Mater. **5**(6), 452–456 (2006)
15. N. Jiménez, O. Umnova, J.-P. Groby (eds.), *Acoustic Waves in Periodic Structures, Metamaterials, and Porous Media*. (Springer, Cham, Switzerland, 2021), p. 12
16. G. Ma, P. Sheng, Acoustic metamaterials: from local resonances to broad horizons. Sci. Adv. **2**(2), e1501595 (2016)
17. M. Yang, P. Sheng, Sound absorption structures: from porous media to acoustic metamaterials. Ann. Rev. Mater. Res. **47**, 83–114 (2017)
18. Y.I. Bobrovnitskii, T. Tomilina, Sound absorption and metamaterials: a review. Acoust. Phys. **64**(5), 519–526 (2018)
19. C. Lagarrigue, J.-P. Groby, V. Tournat, O. Dazel, O. Umnova, Absorption of sound by porous layers with embedded periodic array of resonant inclusions. J. Acoust. Soc. Am. **134**, 4670 (2013)
20. J.-P. Groby, B. Nennig, C. Lagarrigue, B. Brouard, O. Dazel, V. Tournat, Enhancing the absorption properties of acoustic porous plates by periodically embedding Helmholtz resonators. J. Acoust. Soc. Am. **137**, 273 (2015)
21. C. Lagarrigue, J.-P. Groby, O. Dazel, V. Tournat, Design of metaporous supercells by genetic algorithm for absorption optimization on a wide frequency band. Appl. Acoust. **102**, 49 (2016)
22. X. Cai, Q. Guo, G. Hu, J. Yang, Ultrathin low-frequency sound absorbing panels based on coplanar spiral tubes or coplanar Helmholtz resonators. Appl. Phys. Lett. **105**(12), 121901 (2014)
23. Y. Li, B.M. Assouar, Acoustic metasurface-based perfect absorber with deep subwavelength thickness. Appl. Phys. Lett. **108**(6), 063502 (2016)
24. J.-P. Groby, R. Pommier, Y. Aurégan, Use of slow sound to design perfect and broadband passive sound absorbing materials. J. Acoust. Soc. Am. **139**(4), 1660–1671 (2016)
25. Y. Wang, H. Zhao, H. Yang, J. Zhong, J. Wen, A space-coiled acoustic metamaterial with tunable low-frequency sound absorption. EPL (Europhys. Lett.) **120**(5), 54001 (2018)
26. C. Shen, S.A. Cummer, Harnessing multiple internal reflections to design highly absorptive acoustic metasurfaces. Phys. Rev. Appl. **9**(5), 054009 (2018)
27. Z. Yang, J. Mei, M. Yang, N. Chan, P. Sheng, Membrane-type acoustic metamaterial with negative dynamic mass. Phys. Rev. Lett. **101**(20), 204301 (2008)

28. V. Romero-García, G. Theocharis, O. Richoux, A. Merkel, V. Tournat, V. Pagneux, Perfect and broadband acoustic absorption by critically coupled sub-wavelength resonators. Sci. Rep. **6**, 19519 EP–, 01 (2016)
29. X. Guo, V. Gusev, K. Bertoldi, V. Tournat, Manipulating acoustic wave reflexion by a nonlinear elastic metasurface. J. App. Phys. **123**(12), 124901 (2018)
30. X. Guo, V. Gusev, V. Tournat, B. Deng, K. Bertoldi, Frequency-doubling effect in acoustic reflection by a nonlinear, architected rotating-square metasurface. Phys. Rev. E **99**, 052209 (2019)
31. M. Law, L.E. Greene, J.C. Johnson, R. Saykally, P. Yang, Nanowire dye-sensitized solar cells. Nat. Mater. **4**(6), 455–459 (2005)
32. A. Derode, P. Roux, M. Fink, Robust acoustic time reversal with high-order multiple scattering. Phys. Rev. Lett. **75**(23), 4206 (1995)
33. Y. Chong, L. Ge, H. Cao, A.D. Stone, Coherent perfect absorbers: time-reversed lasers. Phys. Rev. Lett. **105**(5), 053901 (2010)
34. K.Y. Bliokh, Y.P. Bliokh, V. Freilikher, S. Savel'ev, F. Nori, Colloquium: unusual resonators: plasmonics, metamaterials, and random media. Rev. Mod. Phys. **80**(4), 1201 (2008)
35. V. Romero-García, G. Theocharis, O. Richoux, V. Pagneux, Use of complex frequency plane to design broadband and sub-wavelength absorbers. J. Acoust. Soc. Am. **139**(6), 3395–3403 (2016)
36. G. Ma, M. Yang, S. Xiao, Z. Yang, P. Sheng, Acoustic metasurface with hybrid resonances. Nat. Mater. **13**(9), 873–878 (2014)
37. M. Yang, C. Meng, C. Fu, Y. Li, Z. Yang, P. Sheng, Subwavelength total acoustic absorption with degenerate resonators. Appl. Phys. Lett. **107**(10), 104104 (2015)
38. Y. Aurégan, Ultra-thin low frequency perfect sound absorber with high ratio of active area. Appl. Phys. Lett. **113**(201904) (2018)
39. M. Malléjac, A. Merkel, J. Sánchez-Dehesa, J. Christensen, V. Tournat, J.-P. Groby, V. Romero-García, Zero-phase propagation in realistic plate-type acoustic metamaterials. Appl. Phys. Lett. **115**(13), 134101 (2019)
40. M. Malléjac, A. Merkel, V. Tournat, J.-P. Groby, V. Romero-García, Doping of a plate-type acoustic metamaterial. Phys. Rev. B **102**, 060302 (2020)
41. J.-P. Groby, W. Huang, A. Lardeau, Y. Aurégan, The use of slow waves to design simple sound absorbing materials. J. Appl. Phys. **117**(12), 124903 (2015)
42. J. Boulvert, J. Costa-Baptista, T. Cavalieri, V. Romero-García, G. Gabard, E.R. Fotsing, A. Ross, M. Perna, J. Mardjono, J.-P. Groby, Folded metaporous material for sub-wavelength and broadband perfect sound absorption. Appl. Phys. Lett. **117**(25), 251902 (2020)
43. V. Leroy, A. Strybulevych, M. Lanoy, F. Lemoult, A. Tourin, J.H. Page, Superabsorption of acoustic waves with bubble metascreens. Phys. Rev. B **91**, 020301 (2015)
44. A.A. Fernández-Marín, N. Jiménez, J.-P. Groby, J.Sánchez-Dehesa, V. Romero-García, Aerogel-based metasurfaces for perfect acoustic energy absorption (2019). arXiv:1906.04496v2
45. H. Long, Y. Cheng, J. Tao, X. Liu, Perfect absorption of low-frequency sound waves by critically coupled subwavelength resonant system. Appl. Phys. Lett. **110**(2), 023502 (2017)
46. J. Boulvert, T. Cavalieri, J. Costa-Baptista, L. Schwan, V. Romero-García, G. Gabard, E.R. Fotsing, A. Ross, J. Mardjono, J.-P. Groby, Optimally graded porous material for broadband perfect absorption of sound. J. Appl. Phys. **126**(17), 175101 (2019)
47. N. Jiménez, W. Huang, V. Romero-García, V. Pagneux, J.-P. Groby, Ultra-thin metamaterial for perfect and quasi-omnidirectional sound absorption. Appl. Phys. Lett. **109**(12), 121902 (2016)
48. N. Jiménez, V. Romero-García, V. Pagneux, J.-P. Groby, Quasiperfect absorption by subwavelength acoustic panels in transmission using accumulation of resonances due to slow sound. Phys. Rev. B **95**, 014205 (2017)
49. N. Jiménez, V. Romero-García, V. Pagneux, J.-P. Groby, Rainbow-trapping absorbers: broadband, perfect and asymmetric sound absorption by subwavelength panels for transmission problems. Sci. Rep. **7**(1), 13595 (2017)

50. N. Jiménez, T.J. Cox, V. Romero-García, J.-P. Groby, Metadiffusers: deep-subwavelength sound diffusers. Sci. Rep **7**(1), 5389 (2017)
51. N. Jiménez, V. Romero-García, J.-P. Groby, Perfect absorption of sound by rigidly-backed high-porous materials. Acta Acustica United Acustica **104**(3), 396–409 (2018)
52. A. Merkel, G. Theocharis, O. Richoux, V. Romero-García, V. Pagneux, Control of acoustic absorption in one-dimensional scattering by resonant scatterers. Appl. Phys. Lett. **107**(24), 244102 (2015)
53. V. Achilleos, O. Richoux, and G. Theocharis, Coherent perfect absorption induced by the nonlinearity of a Helmholtz resonator. J. Acoust. Soc. Am. **140**(EL94) (2016)
54. H. Long, Y. Cheng, X. Liu, Asymmetric absorber with multiband and broadband for low-frequency sound. Appl. Phys. Lett. **111**(14), 143502 (2017)
55. A. Merkel, V. Romero-García, J.-P. Groby, J. Li, J. Christensen, Unidirectional zero sonic reflection in passive pt-symmetric Willis media. Phys. Rev. B **98**(201102(R)) (2018)
56. E. Monsalve, A. Maurel, P. Petitjeans, V. Pagneux, Perfect absorption of water waves by linearor nonlinear critical coupling. Appl. Phys. Lett. **114**(013901) (2018)
57. L. Schwan, O. Umnova, C. Boutin, Sound absorption and reflection from a resonant metasurface: Homogenisation model with experimental validation. Wave Motion **72**, 154–172 (2017)
58. S. Huang, X. Fang, X. Wang, B. Assouar, Q. Cheng, Y. Li, Acoustic perfect absorbers via spiral metasurfaces with embedded apertures. Appl. Phys. Lett. **113**(23), 233501 (2018)
59. A. Elayouch, M. Addouche, A. Khelif, Extensive tailorability of sound absorption using acoustic metamaterials. J. Appl. Phys. **124**(15), 155103 (2018)
60. A. Maurel, J.-F. Mercier, K. Pham, J.-J. Marigo, A. Ourir, Enhanced resonance of sparse arrays of Helmholtz resonators–application to perfect absorption. J. Acoust. Soc. Am. **145**(4), 2552–2560 (2019)
61. V. Romero-García, N. Jiménez, J.-P. Groby, A. Merkel, V. Tournat, G. Theocharis, O. Richoux, V. Pagneux, Perfect absorption in mirror-symmetric acoustic metascreens. Phys. Rev. Appl. **14**(054055) (2020)
62. J. Boulvert, G. Gabard, V. Romero-García, J.-P. Groby, Compact resonant systems for perfect and broadband sound absorption in wide waveguides in transmission problems. Sci. Rep. **12**(1), 10013 (2022)
63. M. Malléjac, P. Sheng, V. Tournat, V. Romero-García, J.-P. Groby, Slow-sound-based delay-line acoustic metamaterial. Phys. Rev. Appl. **17**, 044035 (2022)
64. V. Pagneux, A. Maurel, Scattering matrix properties with evanescent modes for waveguides in fluids and solids. J. Acoust. Soc. Am. **116**(4), 1913–1920 (2004)
65. R. Carminati, J.J. Sáenz, J.-J. Greffet, M. Nieto-Vesperinas, Reciprocity, unitarity, and time-reversal symmetry of the s matrix of fields containing evanescent components. Phys. Rev. A **62**, 012712 (2000)
66. C.P.A. Wapenaar, Reciprocity theorems for two-way and one-way wave vectors: A comparison. J. Acoust. Soc. Am. **100**(6), 3508–3518 (1996)
67. Y. Chong, L. Ge, H. Cao, A. Stone, Coherent perfect absorbers: time-reversed lasers. Phys. Rev. Lett. **105**, 053901 (2010)
68. P. Wei, C. Croënne, S.T. Chu, J. Li, Symmetrical and anti-symmetrical coherent prefect absorption for acoustic waves. Appl. Phys. Lett. **104**, 121902 (2014)
69. N. Jiménez, V. Romero-García, J.-P. Groby, Perfect absorption of sound by rigidly-backed high-porous materials. Acta Acustica United Acustica **104**(3), 396–409 (2018)
70. A. Moroz, A.E. Miroshnichenko, On beautiful analytic structure of the s-matrix. New J. Phys. **21**, 103035 (2019)
71. V. Pagneux, Trapped modes and edge resonances in acoustics and elasticity, in *Dynamic Localization Phenomena in Elasticity, Acoustics and Electromagnetism*, vol. 547 (ISM International Centre for Mechanical Sciences, Springer, Vienna, 2013), pp.181–223
72. G. Theocharis, O. Richoux, V. Romero-Garcìa, A. Merkel, V. Tournat, Limits of slow sound and transparency in lossy locally resonant periodic structures. New J. Phys. **16**, 093017 (2014)
73. L. Barguet, V. Romero-García, N. Jiménez, L.M. Garcia-Raffi, V.J. Sánchez-Morcillo, J.P. Groby, Natural sonic crystal absorber constituted of seagrass (posidonia oceanica) fibrous spheres. Sci. Rep. **11**(1), 711 (2021)

74. Y. Meng, V. Romero-García, G. Gabard, J.-P. Groby, C. Bricault, S. Goudè, Subwavelength broadband perfect absorption for unidimensional open-duct problems. Adv. Mater. Technol. **8**, 2201909 (2023)